PAPER

Tunable construction of CuS nanosheets@flower-like ZnCo-layered double hydroxide nanostructures for hybrid supercapacitors†

Akbar Mohammadi Zardkhoshoui,*
Ramtin Arian and Saied Saeed Hosseiny Davarani [iD] *

Layered double hydroxides (LDHs) are regarded as ideal materials for supercapacitors due to their excellent electrochemical characteristics and unique structural properties. However, unsatisfactory cyclability and poor conductivity have been recognized as the key limitations to LDH performance. To overcome these obstacles, constructing hybrid materials as well as designing porous nanoarchitectures are efficient approaches. Herein, through controlling the sulfide ion concentration during the synthesis of CuS nanosheets and adjusting the amount of urea in the synthesis of flower-like ZnCo-LDH structures, an optimized sample with an exclusive porous texture was fabricated on nickel foam (NF) (identified as NF@CS10-ZC-LDH4) *via* two-step hydrothermal routes and then employed as a binder-less electrode for a hybrid supercapacitor. The as-fabricated nanoarchitectures provide efficient electron-ion transport channels and preserve the structural integrity during prolonged periods of cycling, which resulted in fantastic supercapacitive properties with a capacity of 1270.5 C g^{-1} and excellent cyclability (remaining at 90.7% after 7000 cycles). Furthermore, we fabricated a hybrid supercapacitor (NF@CS10-ZC-LDH4// NF@AC) with NF@CS10-ZC-LDH4 as a cathode electrode and activated carbon (AC)-covered NF as an anode electrode. The energy density of NF@CS10-ZC-LDH4//NF@AC was high, at 62.4 W h kg^{-1} with a power density of 810.4 W kg^{-1} and splendid cyclability of 88.4%. This innovative study offers valuable inspiration for the synthesis of electrode materials to be used in hybrid supercapacitors.

1 Introduction

The overexploitation of fossil fuels has created substantial problems, such as diseases, undesirable changes in the weather and global ecology, and environmental pollution.[1,2] Natural energy sources such as tidal, solar, and wind energy have been exploited as an alternative to fossil fuels.[3,4] Nevertheless, an irregular distribution of these energy sources due to geographical, temporal, and seasonal obstacles has largely restricted their direct use in industry and daily life.[3,4] Accordingly, green, low-cost, and efficient energy storage systems with satisfactory properties are particularly vital for energy harvesting.[5]

Batteries and supercapacitors are popular candidates for energy storage systems. Supercapacitors present the merits of satisfactory power performance, rapid charging, and outstanding longevity despite low energy density, whereas batteries reflect splendid energy density properties despite unsatisfactory power performance.[6–10] Hybrid supercapacitors can combine the advantages of batteries and supercapacitors without attenuating the cycle durability and power density of supercapacitors to obtain a satisfactory energy density.[11–14] Designing suitable battery-like electrode materials is the key method that will improve the performance of hybrid supercapacitors.[15–18]

Metal sulfides (MSs) have been gaining serious attention owing to their good theoretical capacity and desired conductivity.[19–21] Among these MSs, copper sulfide (CuS) has attracted great attention due to its good conductivity and electrochemical performance.[22,23] For instance, Zhou *et al.* reported CuS nanoflake arrays on carbon cloth using a solvothermal strategy, and obtained a capacity of 213.8 C g^{-1} with a longevity of 75.1% after 5000 cycles.[24] In another study, Li *et al.* prepared porous CuS nanosheets *via* a

Department of Chemistry, Shahid Beheshti University, G. C., 1983963113, Evin, Tehran, Iran. E-mail: mohammadi.bahadoran@gmail.com, ss-hosseiny@sbu.ac.ir; Fax: +98 21 22431661; Tel: +98 21 22431661

solvothermal process, which exhibited a capacitance of 974 F g^{-1} and durability of 81.99% after 5000 cycles.[25] Nonetheless, the longevity and specific capacity of CuS are unsatisfactory due to its inferior conductivity, which limits its utilization in supercapacitors.[26] For this reason, it is crucial to combine other materials that possess good theoretical capacity with CuS to enhance its performance.

Recently, layered double hydroxides (LDHs) have been extensively utilized in the preparation of electrode materials for supercapacitors due to their large specific area, adjustable chemical composition, low cost, multiple oxidation states, good theoretical capacity, and flexible anion exchange.[27,28] Considering the plentiful abundance of zinc (Zn) resources and rich redox reactions of ZnCo-LDH, ZnCo-LDH should be a very promising material for future use in a supercapacitor.[29] It has been proved that the incorporation of elemental Zn in cobalt hydroxide can enhance its electrochemical performance.[30] In the ZnCo-LDH material, elemental Co increases the electronic conductivity, and the elemental Zn possesses reasonable electrical conductivity that can result in the enhancement of electrical conductivity and supercapacitive performance.[31,32] Zn ions also improve the interaction between the reactants and electroactive sites throughout the electrochemical redox reactions, thereby enhancing the electrochemical performance of the sample.[27,33]

Nano-structurization is an efficient strategy that boosts the supercapacitive performance of materials. Various morphologies such as nanorods,[34] nanoparticles,[35] nanowires,[36] nanosheets,[37] and flower-like structures[38] have been designed and used in supercapacitors. Generally, powdered materials are prepared via co-precipitation or hydrothermal processes that require polymer binders, resulting in low conductivity and poor stability.[39] To solve the above-mentioned limitations, the rational fabrication of nanocomposites with various hierarchical morphologies and structures has been performed, especially those in the form of nanosheets or flowers that are directly grown on conductive substrates to boost the conductivity and so enhance the electrochemical features.[32,33] The three-dimensional (3D) nanostructures can accelerate the transport of electrons and ions by increasing the active areas in contact with the electrolyte.[17] For example, Li et al. reported a hydrothermal strategy that produced flower-like MnO_2–NiFe LDH nanosheets on nickel foam (NF), which showed a capacitance of 4274.4 mF cm^{-2} at 5 mA cm^{-1} and longevity of 95.6%.[40] In another work, Raza et al. used a hydrothermal process to fabricate flower-like NiMn-LDH-$MnCo_2S_4$, with a capacity of 1228 C g^{-1} and a cyclability of 95%.[41]

Herein, CuS nanosheets coupled with flower-like ZnCo-LDH nanostructures supported on NF (NF@CS-ZC-LDH) were synthesized for the hybrid supercapacitor. Compared with the NF@CS and NF@ZC-LDH electrodes, NF@CS-ZC-LDH exhibited a more optimal supercapacitor performance due to the porous architecture and the synergy of CuS, ZnCo-LDH,

and NF. Moreover, a hybrid supercapacitor (NF@CS-ZC-LDH// NF@AC) was fabricated and revealed an excellent performance. This study is expected to pave the way for new insights into the construction of binder-less electrodes for various applications.

2 Experimental section

2.1 Chemicals

Herein, the chemicals used were C_3H_6O [acetone], $Cu(NO_3)_2 \cdot 6H_2O$ [copper(II) nitrate hexahydrate], $Na_2S_2O_3 \cdot 5H_2O$ [sodium thiosulfate pentahydrate], $Co(NO_3)_2 \cdot 6H_2O$ [cobalt(II) nitrate hexahydrate], $Zn(NO_3)_2 \cdot 6H_2O$ [zinc nitrate hexahydrate], CH_4N_2O [urea], and C_2H_6O [ethanol].

2.2 Fabrication of the NF@CS electrode

First, the NF was cut into a rectangular piece 2×4 cm^2 in size. Then, the oxide layer and oil on its surface were removed with sequential ultrasonication in C_3H_6O, HCl (1.0 M), and then water, and subsequently dried in a vacuum oven at 60 °C.[42] To fabricate the CuS nanosheets on the NF, $Cu(NO_3)_2 \cdot 6H_2O$ (10 mmol) and $Na_2S_2O_3 \cdot 5H_2O$ (10 mmol) were dissolved in water (100 mL) under stirring for 1 h to form a homogenous solution. The mixture was transferred into an autoclave with pretreated NF vertically placed in it and heated in an oven at 90 °C for 6 h. Finally, the NF covered with CuS was cleaned numerous times with C_2H_6O and water and then dried at 50 °C for 12 h to obtain the NF@CS10.

The mass of the CuS sample grown on the NF was obtained by subtracting the bare NF mass from that of the fabricated CuS-loaded NF. The mass loading of CuS was estimated to be 2.1 mg cm^{-2}. Also, two sulfide samples with different concentrations of $Na_2S_2O_3 \cdot 5H_2O$ (5 and 15 mmol) were synthesized under similar conditions, and were marked as NF@CS5 and NF@CS15, respectively. The mass of CS5 and CS15 on NF was calculated to be 1.9 and 2.4 mg cm^{-2}, respectively.

2.3 Fabrication of the NF@CS10-ZC-LDH electrode

NF@CS10 was used as a framework for the growth of flower-like ZnCo-LDH structures via a second hydrothermal process. Typically, $Zn(NO_3)_2 \cdot 6H_2O$ (1 mmol), $Co(NO_3)_2 \cdot 6H_2O$ (4 mmol), and CH_4N_2O (4 mmol) were dissolved in water (60 mL) and stirred for 20 min. Then, the solution was transferred into an autoclave with NF@CS10 vertically placed in it and maintained at 120 °C for 12 h. Next, the sample named NF@CS10-ZC-LDH4 was washed with water and C_2H_6O and heated for 14 h at 50 °C in a drying oven. For comparison, two products with 2 and 6 mmol of CH_4N_2O were also fabricated using the same method, which were named NF@CS10-ZC-LDH2 and NF@CS10-ZC-LDH6, respectively. The mass values of CS10-ZC-LDH2, CS10-ZC-LDH4, and CS10-ZC-LDH6 on the NF were observed to be 3.8, 4.1, and 4.7 mg cm^{-2}, respectively. Pure NF@ZC-LDH4 was also

fabricated without adding $Cu(NO_3)_2 \cdot 6H_2O$ and $Na_2S_2O_3 \cdot 5H_2O$. The mass of ZC-LDH4 on the NF was estimated to be 2 mg cm^{-2}.

2.4 Characterization techniques

To prevent the NF from affecting the samples, the as-prepared products were carefully stripped from the NF using a clean knife and then collected for XRD, TEM, XPS, and BET analyses. The morphology of the as-synthesized products was examined using field-emission scanning electron microscopy (FE-SEM) (MIRA 3 TESCAN, 15 kV, Czech) and transmission electron microscopy (TEM) (Philips CM200 instrument). The crystallographic information for CS10-ZC-LDH4 was further analyzed by X-ray diffraction (XRD) (Philips X'Pert Pro X-ray diffractometer). The elemental valance states of CS10-ZC-LDH4 were identified using an X-ray photoelectron spectrometer (XPS) (Thermo Scientific, ESCALAB 250Xi, Mg X-ray source). The pore-size distribution and specific surface area (SSA) of CS10, ZC-LDH4, and CS10-ZC-LDH4 were evaluated by the Barrett–Joyner–Halenda (BJH) model and Brunauer–Emmett–Teller (BET) surface area, respectively.

2.5 Electrochemical tests

2.5.1 Three-electrode cell. Electrochemical techniques such as cyclic voltammetry (CV), galvanostatic charge–discharge (GCD), and electrochemical impedance spectroscopy (EIS) were performed using an Autolab PGSTAT 204 (Eco Chemie, The Netherlands) at room temperature in 6.0 M KOH electrolyte. The three-electrode cell consisted of a counter electrode (Pt wire), a reference electrode (Ag/AgCl), and a working electrode. Herein, the as-prepared materials on the NF were directly employed as the working electrode. The NF was utilized as an electrode substrate because of its excellent conductivity as well as its multi-dimensional texture to support materials.[43] Of note, the capacity value (C, C g^{-1}) of electrodes was calculated from the equation $C = I\Delta t/m$, where m (g), Δt (s), and I (A) denote the mass of the samples, discharge time, and applied working current, respectively.[44]

2.5.2 Assembly of the NF@CS-ZCLDH//NF@AC device. A hybrid supercapacitor (NF@CS10-ZCLDH4//NF@AC) containing NF@CS10-ZCLDH4 as the cathode, NF@AC as the anode, one piece of filter paper as a separator, and KOH (6.0 M) as the electrolyte was fabricated and tested in a two-electrode configuration. Typically, the anode was fabricated by mixing 80% activated carbon (AC), 10% acetylene black, and 10% polyvinylidene fluoride in the proper amount of N-methyl-2-pyrrolidone solvent to generate a slurry. To coat AC on the NF, the NF was immersed in the obtained suspension to form a coating area (1 cm × 1 cm) and then dried overnight. Before the fabrication of NF@CS10-ZCLDH4//NF@AC, the electrodes and filter paper were soaked in KOH to obtain the best performance of the device.[43] Subsequently, the components of NF@CS10-ZCLDH4//NF@AC were carefully sealed in a non-conductive bag using a heat sealer to construct NF@CS10-ZCLDH4//NF@AC. It should be noted that the working area of the device was 1 × 1 cm.

To obtain high efficiency for NF@CS10-ZCLDH4//NF@AC, the charges for the device were balanced. The cathode and anode electrodes were balanced according to the charge balance theory ($Q_+ = Q_-$), which follows the relationship $m_+ \times C_+ = m_- \times C_- \times \Delta V_-$, where m_- (g) and m_+ (g) represent the mass values of the AC and CS10-ZCLDH4 on the NF, respectively. ΔV_- indicates the potential window of NF@AC, and C_- (F g^{-1}) and C_+ (C g^{-1}) reveal the capacitance and capacity of NF@AC and NF@CS10-ZCLDH4, respectively. Accordingly, the mass values of the NF@CS10-ZCLDH4 and NF@AC electrodes in NF@CS10-ZCLDH4//NF@AC were 4.1 and 28.3 mg, respectively. The energy density (E_d, W h kg^{-1}) and power density (P_d, W kg^{-1}) of NF@CS10-ZCLDH4//NF@AC can easily be evaluated from the following equations:[45]
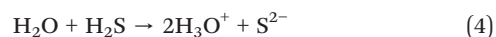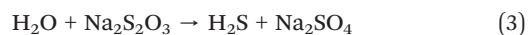
$$E_d \left(W\ h\ kg^{-1} \right) = \frac{I\int V dt}{3.6 \times M} \tag{1}$$

$$P_d \left(W\ kg^{-1} \right) = \frac{E}{\Delta t} \times 3600 \tag{2}$$

In eqn (1), M indicates the total mass of materials, and Δt represents the discharging time.

3 Results and discussion

Flower-like ZC-LDH4 structures were directly formed on the NF@CS10 nanosheets through a hydrothermal reaction, as evidenced in Fig. 1, where NF was applied as the template due to its 3D porous texture and excellent electronic conductivity.[43] The CuS nanostructures were firmly grown on the NF after the hydrothermal reaction (step I). During the hydrothermal process, $Na_2S_2O_3$ reacted with H_2O to generate H_2S. Then, Cu^{2+} reacted with H_2S to form CuS nanosheets. The related reactions for the formation of CuS nanosheets can be demonstrated as follows:[46]

$$H_2O + Na_2S_2O_3 \rightarrow H_2S + Na_2SO_4 \tag{3}$$

$$H_2O + H_2S \rightarrow 2H_3O^+ + S^{2-} \tag{4}$$

$$S^{2-} + Cu^{2+} \rightarrow CuS \tag{5}$$

Subsequently, flower-like ZC-LDH4 nanostructures were directly produced on the surface of NF@CS10 to obtain NF@CS10-ZC-LDH4 (step II). Before the hydrothermal reaction, NF@CS10 was soaked in a solution containing Zn^{2+}, Co^{2+}, NO_3^-, and CH_4N_2O in an autoclave. With increasing temperature, CO_3^{2-} and OH^- were generated due to the hydrolysis of CH_4N_2O. The related reactions for the formation of ZC-LDH4 can be reflected as follows:[47]

© 2023 The Author(s). Co-published by the Institute of Process Engineering, Chinese Academy of Sciences and the Royal Society of Chemistry

Ind. Chem. Mater., 2023, **1**, 443–457 | **445**

Fig. 1 Step (I) schematic diagram for the preparation of NF@CS10 nanosheets. Step (II) schematic diagram for the preparation of NF@CS10–ZC–LDH4.

$$H_2O + CO(NH_2)_2 \rightarrow 2NH_3 + CO_2 \quad (6)$$

$$NH_3 \cdot H_2O \rightarrow OH^- + NH_4^+ \quad (7)$$

$$H_2O + CO_2 \rightarrow 2H^+ + CO_3^- \quad (8)$$

$$(1-x)Zn^{2+} + xCo^{2+} + 2OH^- \rightarrow (Zn_{1-x}Co_x)(OH)_2 \quad (9)$$

The porous characteristics and morphology of the samples are crucial elements for determining the supercapacitive performance of the materials. Accordingly, the morphological evolution of the samples was initially analyzed using FE-SEM. The morphological changes in the CuS nanostructures, synthesized with three different amounts of $Na_2S_2O_3$ (5, 10, and 15 mmol), were first analyzed through FE-SEM. Fig. S1a (ESI†) shows the morphology of NF@CS5, indicating that the CS5 nanostructures were fully distributed on the NF. The addition of a 5 mmol amount of $Na_2S_2O_3$ created a smooth surface for all the obtained nanosheets on the NF, and these nanosheets did not aggregate together (Fig. S1b–d†). Fig. S1e† shows a low magnification FE-SEM image of NF@CS10, and a great deal of the nanosheets firmly grew on the NF. The enlarged image displayed in Fig. S1f† proved that the surface of the nanosheets changed from smooth to rough and formed a porous architecture, and enlarged images also show that the formed nanosheets possess rich porosity (Fig. S1g and h†).

At a high $Na_2S_2O_3$ concentration (NF@CS15), as observed in Fig. S1i–l,† over-sulfidation of the sample crushed the nanosheets and also collapsed the structure, causing significant agglomeration on the NF. The CS10 nanosheets offer numerous anchoring sites for ZC-LDH nanostructures to grow, which consequently resulted in hybrid material with a flower-like architecture. Accordingly, after the second hydrothermal process, flower-like ZC-LDH nanostructures developed on the surface of the CS10 nanosheets to form NF@CS10-ZC-LDH4. Here, another hydrothermal route at a constant temperature with the addition of three amounts of CH_4N_2O was used to obtain different morphologies.

The surface morphology of the ZC-LDH samples with three amounts of CH_4N_2O (2, 4, and 6 mmol) on NF@CS10 (NF@CS10-ZC-LDH2, NF@CS10-ZC-LDH4, and NF@CS10-ZC-LDH6) was studied by FE-SEM. The FE-SEM image in Fig. 2a indicates that the NF was uniformly covered with CS10-ZC-LDH2 hybrid arrays. Fig. 2b and c show that the ZC-LDH2 structures were deposited on the NF@CS10 nanosheets in the form of rose flower-like architectures. At this time, the surface of the rose flower-like structures is relatively smooth (Fig. 2d). It was determined from the FE-SEM image of one single rose flower that the thickness of the nano-petals is ≈31 nm (Fig. 2d).

After the addition of a 4 mmol amount of CH_4N_2O, the NF@CS10 surface was still covered with ZC-LDH4 on a large scale (Fig. 2e). In addition, the sample (Fig. 2f and g) obtained by adding a 4 mmol amount of CH_4N_2O maintained the flower-like architecture but revealed a rougher surface than that of the NF@CS10-ZC-LDH2. The roughness on the surface of the structure effectively increased the surface area and porosity of the CS10-ZC-LDH4 heterostructure.[48] Nevertheless, each nano-petal of the flower became slightly thicker, with a thickness of 44 nm (Fig. 2h). More significantly, the nanoflowers of NF@CS10-ZnCo-LDH4 were more compact in structure than those of NF@CS10-ZC-LDH2, which not only accelerates charge transfer and ion diffusion but also efficiently provides additional reaction sites to

Fig. 2 (a–d) FE-SEM images of NF@CS10-ZC-LDH2. (e–h) FE-SEM images of NF@CS10-ZC-LDH4. (i–l) FE-SEM images of NF@CS10-ZC-LDH6.

Fig. 3 (a and b) TEM images of the CS10 sample. (c and d) TEM image of the CS10-ZC-LDH4 sample.

© 2023 The Author(s). Co-published by the Institute of Process Engineering, Chinese Academy of Sciences and the Royal Society of Chemistry

Ind. Chem. Mater., 2023, **1**, 443–457 | **447**

significantly improve the electrical activities of NF@CS10-ZC-LDH4.[48]

CS10-ZC-LDH6 showed uniformly grown spherical-like structures throughout the NF (Fig. 2i). Fig. 2j–l shows that when the added amount of CH_4N_2O was increased to 6 mmol, the morphology changed from flower-like structures to spherical-like structures, and the spheres were decorated with particles. Also, the CS10 nanosheets were not visible due to significant agglomeration and accumulation of the spheres. It is worth noting that the nano-petals on the surface of the flower tended to disappear when the amount of CH_4N_2O reached 6 mmol (Fig. 2j–l). The morphology of NF@CS10-ZC-LDH4 was more regular as compared to other products, while the petals of the NF@CS10-ZC-LDH6 flowers revealed evident collapse. According to the FE-SEM analysis, it can be concluded that the porous surface of the CS10 nanosheets and flower-like ZC-LDH4 structures after adhering provides stable and appropriate channels to reduce the electrode–electrolyte resistance.[48] As highlighted in the FE-SEM mapping (Fig. S2a–f†), Cu, S, Zn, Co, and O coexisted and were distributed in NF@CS10-ZC-LDH4, which further affirmed the successful fabrication of NF@CS10-ZC-LDH4. For comparison, the FE-SEM images of pure ZC-LDH4 shown in Fig. S3† indicate that the surface of the NF was covered by flower-like ZnCo-LDH4 arrays.

The detailed intrinsic morphological features of CS10 and CS10-ZC-LDH4 were further confirmed by TEM analysis (Fig. 3). For the TEM investigation, the NF surface was

carefully scraped, and the collected powder was dispersed in C_2H_5OH. The sample solution was drop-cast onto the TEM grid. The TEM image of the CS10 sample confirmed the sheet-like structure of CS10 (Fig. 3a), which is in reasonable agreement with its FE-SEM image. As demonstrated in Fig. 3b, the edge layer of the nanosheets is reliable evidence of the porous texture of CS10. The TEM images of CS10-ZC-LDH4 (Fig. 3c and d) indicated that two different morphological structures, consisting of CS10 nanosheets and flower-like CS10-ZC-LDH4 structures, were coupled together to create a hybrid CS10-ZC-LDH4 heterostructure, which revealed an absolute resemblance to that of the FE-SEM images (Fig. 2e–h). The CS10 texture for growing ZC-LDH4 nanostructures assisted in the rapid transportation of the charge carriers. The ZC-LDH4 nanoflowers also contributed to the improved performance of CS10-ZC-LDH4, with its porous structure.[49]

The crystallinity of CS10-ZC-LDH4 was assessed by XRD analysis (Fig. 4a). The XRD of CS10-ZC-LDH4 revealed diffraction peaks of CuS (JCPDS 06-0464) and ZnCo-LDH (JCPDS 21-1477). The CuS presented signals at 27.66° (101), 29.31° (102), 31.81° (103), 32.71° (006), 47.86° (110), 52.62° (108), and 59.21° (116).[50] There were obvious signals for ZnCo-LDH4 at 21.81° (−111), 26.06° (−113), 28.41° (020), 33.62° (200), 37.26° (024), and 58.36° (−322).[51]

XPS measurements were also implemented to scrutinize the different oxidation states of elements in CS10-ZC-LDH4, as highlighted in Fig. 4b–f. The survey scan in Fig. S4† shows

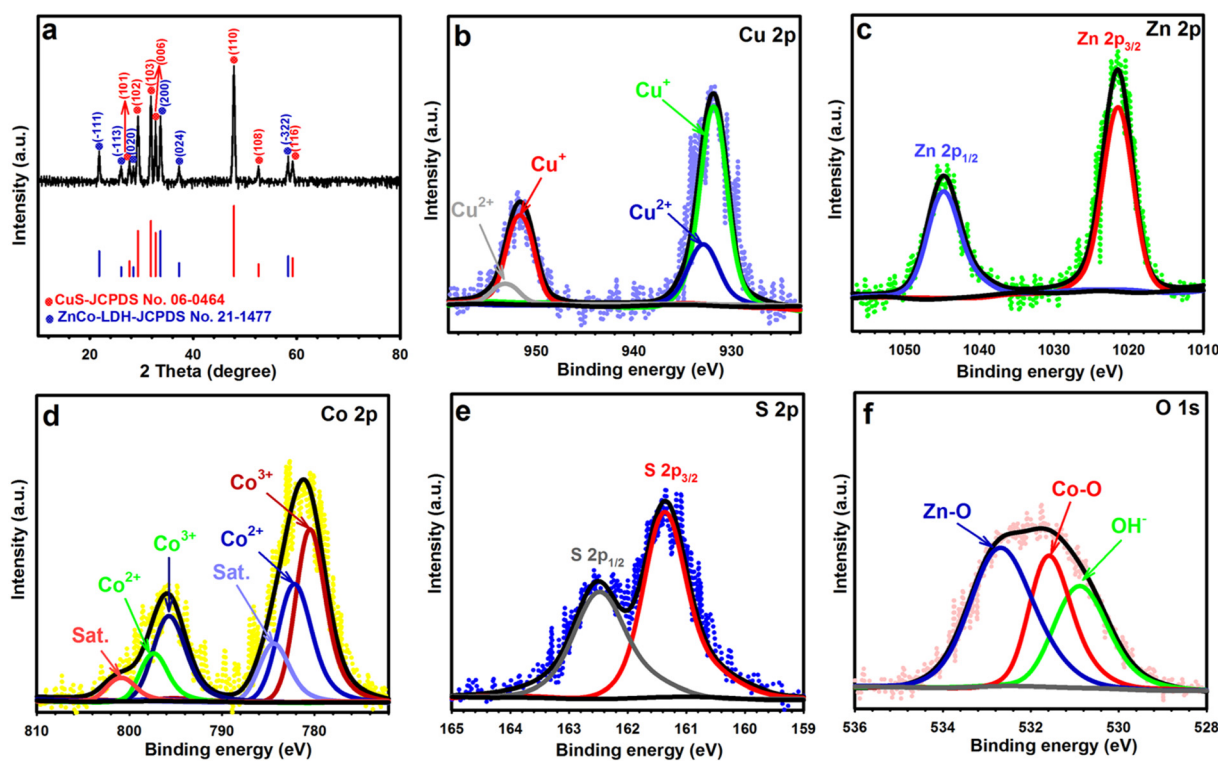

Fig. 4 (a) XRD pattern of CS10-ZC-LDH4. (b) Cu 2p XPS spectra of CS10-ZC-LDH4. (c) Zn 2p XPS spectra of CS10-ZC-LDH4. (d) Co 2p XPS spectra of CS10-ZC-LDH4. (e) S 2p XPS spectra of CS10-ZC-LDH4. (f) O 1s XPS spectra of CS10-ZC-LDH4.

that Cu, S, Zn, Co, and O were explicitly identified in CS10-ZC-LDH4. The Cu 2p spectrum in Fig. 4b revealed two well-resolved signals at 931.88 and 951.68 eV that were assigned to Cu$^+$, while the other two signals at 932.98 and 953.18 eV were predominant signals of Cu^{2+}, which were consistent with previous studies.[23] Fig. 4c shows the spectrum of the Zn 2p, which possesses two evident 2p$_{1/2}$ and 2p$_{3/2}$ peaks at 1044.75 eV and 1021.55 eV, respectively, and strongly supports the presence of Zn^{2+} in CS10-ZC-LDH4.[52] In the Co 2p pattern illustrated in Fig. 4d, the peaks at 780.65 and 795.75 eV were derived from Co^{2+}, and the characteristic peaks at 782.37 and 797.45 eV originated from Co^{3+}. Additionally, satellite peaks (Sat.) were observed at 784.6 and 801.1 eV.[53] Likewise, the peaks at 161.38 and 162.52 eV in the S 2p pattern (Fig. 4e) were attributed to 2p$_{3/2}$ and 2p$_{1/2}$, respectively, reflecting the presence of S^{2-} in CS10-ZC-LDH4.[54] Also, the O 1s (Fig. 4f) was split into three noticeable signals at 530.95, 531.65, and 532.77 eV, which corresponded to bound hydroxide groups, metal–oxygen bonds, and adsorbed water molecules, respectively.[52]

To further explore the porous features and SSA of CS10, ZC-LDH4, and CS10-ZC-LDH4, N$_2$ adsorption/desorption analysis was performed, and the results are sketched in Fig. S5.† From the isotherms of the three samples plotted in Fig. S5,† hysteresis loops and typical IV-type features were obtained for the three products, corroborating their mesoporous nature.[55,56] Inspiringly, the estimated BET surface area of the CS10-ZC-LDH4 was 210.6 m^2 g^{-1}, which was superior to that of ZC-LDH4 (98.8 m^2 g^{-1}) and CS10 (64.7 m^2 g^{-1}) (Fig. S5a–c†). The relevant pore size distribution of CS10, ZC-LDH4, and CS10-ZC-LDH4 was obtained through BJH patterns (Fig. S5d–f†). These proved that the pore sizes of CS10, ZC-LDH4, and CS10@ZC-LDH4 were 7.9, 6.65, and 5.1 nm, respectively, suggesting their mesoporous nature.[55,56] The superior porosity and SSA of CS10-ZC-LDH4 offer abundant active reaction sites and promote electron-ion transport, which is expected to boost the electrochemical performance of CS10-ZC-LDH4.[57,58]
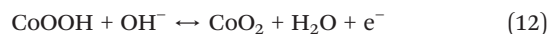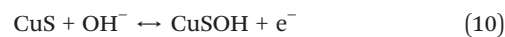
To more accurately evaluate the charge storage ability of the as-designed products, electrochemical characterizations were initially carried out in a three-electrode measuring cell with 6.0 M KOH. Evidence reveals that the specific conductivity of KOH (6.0 M) was relatively higher compared with lower concentrations and thus was more appropriate for enhancing performance.[59,60] For this reason, our team used 6.0 M KOH as a suitable electrolyte. It should be noted that the higher concentration (>6.0 M) was not used due to the peeling of active materials from the surface of the NF.[60,61] Fig. S6a† reveals comparative CV diagrams of the NF@CS5, NF@CS10, and NF@CS15 electrodes at 30 mV s^{-1}. The highest capacity among the three samples was measured for NF@CS10, due to its maximum peak current and largest integral area. Furthermore, the GCD plots for each electrode at 1 A g^{-1} are revealed in Fig. S6b.† The discharge time for NF@CS10 was longer than those of other samples, which demonstrated that it possesses the best capacity

performance. As highlighted in Fig. S6c,† the capacity of NF@CS10 reached 467.5 C g^{-1} at 1 A g^{-1}, which is relatively larger than that of 349 for NF@CS5 and 312 C g^{-1} for NF@CS15.

Considering the above tests, NF@CS10 was selected as the optimized sulfide to improve the performance of NF@ZC-LDH. Fig. S7a and b† show the CV (30 mV s^{-1}) and GCD (1 A g^{-1}) comparison plots for NF@CS10-ZC-LDH2, NF@CS10-ZC-LDH4, and NF@CS10-ZC-LDH6. Compared with NF@CS10-ZC-LDH2 and NF@CS10-ZC-LDH6, the enclosed area in the CV as well as discharge time in GCD for NF@CS10-ZC-LDH4 are the highest at 30 mV s^{-1} and 1 A g^{-1}, respectively, signifying its excellent capacity. This verifies that the porous texture of NF@CS10-ZC-LDH4 benefits the transfer of electrolyte ions and so maximizes the performance. The capacity of NF@CS10-ZC-LDH4 was measured at 1270.5 C g^{-1}, with decreased capacities for NF@CS10-ZC-LDH2 and NF@CS10-ZC-LDH6 at 1184 and 1114.5 C g^{-1}, respectively (Fig. S7c†).

Hence, the NF@CS10-ZC-LDH4 was considered the best electrode among the three samples due to its porous texture. Fig. 5a shows the CV curves for NF, NF@CS10, NF@ZC-LDH4, and NF@CS10-ZC-LDH4 at 30 mV s^{-1}. There was a horizontal line in the CV curve for NF, which confirmed that the excellent capacity of the as-designed electrodes was derived from the presence of active materials on the NF surface.[62] Also, there was a pair of distinct redox peaks for the as-fabricated electrodes, signifying their expected battery-like behaviors. In comparison to NF@CS10 and NF@ZC-LDH4, the positions of the reduction/oxidation peaks for NF@CS10-ZC-LDH4 were slightly shifted towards the more negative and positive potential sides, respectively, due to the differences in the polarization behaviors of the samples.[33,63–66] The polarization behavior of the electrodes is closely related to the physical morphology of the materials.[66] The NF@CS10-ZC-LDH4 electrode revealed enhanced redox peaks and a larger CV-integrated area as compared to other electrodes, reflecting the greater capacity of the electrode. This is due to the larger surface area and richer redox reaction of NF@CS10-ZC-LDH4 from the contribution of each component.[64] The involved faradaic reactions throughout the energy storage process of NF@CS10-ZC-LDH4 can be elaborated as follows:[67–69]

$$CuS + OH^- \leftrightarrow CuSOH + e^- \qquad (10)$$

$$Co(OH)_2 + OH^- \leftrightarrow CoOOH + H_2O + e^- \qquad (11)$$

$$CoOOH + OH^- \leftrightarrow CoO_2 + H_2O + e^- \qquad (12)$$

Note that the Zn in NF@CS10-ZC-LDH4 is not involved in any redox reaction; however, it can allow insertion/deinsertion of K$^+$ ions via forming a double layer at the electrode–electrolyte junction.[33] The relevant GCD plots for NF@CS10, NF@ZC-LDH4, and NF@CS10-ZC-LDH4 investigated at 1 A g^{-1} are illustrated in Fig. 5b. The longest

© 2023 The Author(s). Co-published by the Institute of Process Engineering, Chinese Academy of Sciences and the Royal Society of Chemistry

Ind. Chem. Mater., 2023, 1, 443–457 | 449

Fig. 5 (a) CV curves for pure NF, and the NF@CS10, NF@ZC-LDH4, and NF@CS10-ZC-LDH4 electrodes at 30 mV s^{-1}. (b) GCD curves for the NF@CS10, NF@ZC-LDH4, and NF@CS10-ZC-LDH4 electrodes at 1 A g^{-1}. (c) Specific capacities of the NF@CS10, NF@ZC-LDH4, and NF@CS10-ZC-LDH4 electrodes at 1 A g^{-1}. (d) CV plots for the NF@CS10-ZC-LDH4 electrode from 10 to 50 mV s^{-1}. (e) Linear relationship between cathodic and anodic peaks with the square root of sweep speeds of NF@CS10-ZC-LDH4. (f) Linear relation between the plot of the logarithm (i) *versus* the logarithm (v) of NF@CS10-ZC-LDH4.

discharge time for NF@CS10-ZC-LDH4 demonstrates its higher capacity due to the synergistic interaction between the CS10 nanosheets and ZC-LDH nanoflowers. As estimated from the GCD curves in Fig. 5c, the capacity of NF@CS10-ZC-LDH4 is 1270.5 C g^{-1}, which is greater than that of NF@CS10 (467.5 C g^{-1}) and NF@ZC-LDH4 (836 C g^{-1}) at 1 A g^{-1}. The great capacity of NF@CS10-ZC-LDH4 originates from its exclusive properties, including high SSA, highly porous texture, excellent catalytic activity, and the synergy between CS10 and ZC-LDH4.[64]

The nanosheet-constructed porous architecture can produce copious active sites for the redox reaction and also increase the interfacial contact of the electrode/electrolyte.[70] The resistance behavior of NF@CS10, NF@ZC-LDH4, and NF@CS10-ZC-LDH4 was investigated by the EIS test. The results of the EIS were fitted by employing Z-view software. An appropriate equivalent circuit is represented in Fig. S8 (inset).† The Nyquist plot manifests as a semicircle as well as a sloping direct line in high-frequency and low-frequency zones, respectively. The charge-transfer resistance (marked as R_{ct}) can be indicated by the semicircular diameter.[61,62] The line represents the Warburg diffusion resistance, which reflects the rate of ion diffusion.[7,8] In addition, the intersection with the *x*-axis implies the internal resistance (marked as R_s), which includes the contact resistance between the material and the NF and the intrinsic resistance of the material and electrolyte.[22]

Evidently, NF@CS10-ZC-LDH4 represents the lowest R_s of 0.33 Ω compared with NF@ZC-LDH4 (0.72 Ω) and NF@CS10 (1.2 Ω). Also, the R_{ct} values of NF@CS10-ZC-LDH4, NF@ZC-

LDH4, and NF@CS10 were estimated to be 0.74, 1.30, and 2.45 Ω, respectively. As expected, the R_{ct} of NF@CS10-ZC-LDH4 was substantially smaller than that of NF@CS10, which indicates that ZC-LDH4 structures can increase the conductivity of NF@CS10-ZC-LDH4. Moreover, the straight line of NF@CS10-ZC-LDH4 is the steepest, which indicates its lowest diffusion resistance.

Detailed CV plots of NF@CS10-ZC-LDH4 carried out at several scanning rates (10–50 mV s^{-1}) are shown in Fig. 5d. The redox peaks of NF@CS10-ZC-LDH4 exhibit slight shifts as the sweep speed increases, which can be related to the hindrance of the internal resistance to ion diffusion over the rapid redox process.[70] Additionally, the redox peaks of NF@CS10-ZC-LDH4 continue to be observed at 50 mV s^{-1}, which indicates that the nanosheet-constructed porous architecture is advantageous for boosting rapid faradaic reactions.[70] The CV curves of NF@CS10 and NF@ZC-LDH4 are sketched in Fig. S9.†

To reveal the reaction kinetic characteristics of NF@CS10-ZC-LDH4, the capacitive contribution was examined, which can be determined from the CV graphs. The linear relationship between the square root of the sweep speed ($v^{1/2}$) and the redox peak current (i_p) at various sweep speeds is reflected in Fig. 5e, and demonstrates that the electrochemical process obtained by the NF@CS10-ZC-LDH4 surface was mainly governed by diffusion-controlled reactions.[11–13] The association between the current densities (i) of the cathodic and anodic peaks and the sweep speed (v) is investigated *via* Dunn's formula $i = av^b$,[71] where a and b denote adjustable constants. Importantly, b values of 1 and

Fig. 6 (a) GCD profiles for the NF@CS10-ZC-LDH4 electrode from 1 to 25 A g^{-1}. (b) Specific capacities *vs.* current densities for the NF@CS10, NF@ZC-LDH4, and NF@CS10-ZC-LDH4 electrodes. (c) Comparison of capacity values for NF@CS10-ZC-LDH4 with previously published values. (d) Longevity and coulombic efficiency of NF@CS10-ZC-LDH4 at 5 A g^{-1} (the inset shows FE-SEM images of NF@CS10-ZC-LDH4 after 7000 cycles).

0.5 relate to surface capacitive and diffusion-controlled processes, respectively. Here, the values of b for NF@CS10-ZC-LDH4 are 0.5033 and 0.5038 (Fig. 5f), and correspond to the cathodic peak and anodic peak, respectively, suggesting that the electrochemical kinetics is regulated by ionic diffusion throughout the redox reaction.[11–13]

The GCD plots for NF@CS10-ZC-LDH4 demonstrate the nonlinear states along with features of the faradaic redox reactions as well as battery-like behaviors throughout charge–discharge processes (Fig. 6a). The well-maintained and symmetrical shapes of the GCD plots also verify its satisfactory reversibility. The GCD curves for NF@CS10 and NF@ZC-LDH4 from 1 to 25 A g^{-1} are also indicated in Fig. S10.†

Fig. 6b summarizes the capacity of the three samples, with NF@CS10-ZC-LDH4 representing the maximum capacity at each current density. NF@CS10-ZC-LDH4 presented the capacities of 1270.5, 1240.25, 1127.5, 1067, 957, and 908.4 C g^{-1} at 1, 2.5, 5, 7.5, 15, and 25 A g^{-1}, respectively, which are greater than those of NF@CS10 and NF@ZC-LDH4, and are also greater compared with reported electrodes (Fig. 6c and Table S1 in the ESI†).[72–78] Additionally, the capacities for NF@ZC-LDH4 were 836, 775.5, 721.6, 660, 612.7, and 500 C g^{-1} at the same current densities, respectively, and were larger than that of NF@CS10 (Fig. 6b). Similarly, NF@CS10 demonstrated capacities of 467.5, 396, 336.6, 275, 232.65, and 199.15 C g^{-1} at the same current densities, respectively.

As a crucial indicator, the rate capability of the electrodes was studied. Herein, we compared the capacity retention of NF@CS10, NF@ZC-LDH4, and NF@CS10-ZC-LDH4 from 1 to 25 A g^{-1} (Fig. 6b). Even at 25 A g^{-1}, NF@CS10-ZC-LDH4 maintained 71.5% of its original capacity, which is greater than that of NF@CS10 (42.6%) and NF@ZC-LDH4 (59.8%).

Such a prominent rate performance can be ascribed to its exclusive structure, where the highly porous architecture of NF@CS10-ZC-LDH4 allows electroactive materials to be exposed and contribute to electrochemical reactions.[12,15] In addition, the porous texture facilitates the entrance of the electrolytes and the rapid diffusion of the ions on the surface of the electroactive material.[12,15] These advantages can guarantee a fantastic capacity output, and a satisfactory rate performance will be achieved. Electrochemical cyclability is also crucial for evaluating the performance of the samples. Therefore, the electrochemical cyclability of all products was repeatedly examined *via* GCD for 7000 cycles at 5 A g^{-1}, as evidenced in Fig. 6d. NF@CS10-ZC-LDH4 preserved 90.7% of its capacity after 7000 cycles, whilst NF@ZC-LDH4 and NF@CuS10 retained 81.1%, and 68.7%, respectively (Fig. S11†).

Any decrease in the capacity of the materials during the durability test could be attributed to the dissolution of active materials in the electrolytes or problems in the electrode, such as expansion, corrosion, or loss of active materials due to weak binding.[79] The coulombic efficiency of NF@CS10-ZC-

© 2023 The Author(s). Co-published by the Institute of Process Engineering, Chinese Academy of Sciences and the Royal Society of Chemistry

Ind. Chem. Mater., 2023, **1**, 443–457 | **451**

LDH4 was 98.8% at the end of the cyclability test, which indicated the desired reversibility of NF@CS10-ZC-LDH4 (Fig. 6d). For a greater understanding of the splendid cyclability of NF@CS10-ZC-LDH4, we further explored the NF@CS10-ZC-LDH4 sample after cycling. As shown in Fig. 6d (inset), the morphology analysis of NF@CS10-ZC-LDH4 after 7000 cycles showed no considerable structural variation. The XRD of NF@CS10-ZC-LDH4 (Fig. S12†) revealed that the crystal structure was maintained after cycling 7000 times, which further highlights the satisfactory cyclability of NF@CS10-ZC-LDH4.

Based on the above results, the superior performance of NF@CS10-ZC-LDH4 is generally attributed to the following: (1) the binder-less preparation of NF@CS10-ZC-LDH4 as well as synergy properties of this electrode reduced the internal resistance and then promoted the electrochemical activity for superior capacity;[37] (2) the rich porosity of the composite facilitated rapid electrolyte entry and rapid ion diffusion within materials;[44] (3) the direct growth of the flower-like ZC-LDH4 structures over the CS10 nanosheet created a 3D texture that allowed rapid electron transport between the CS10 nanosheet and the flower-like ZC-LDH4 structures;[37] (4) the presence of elemental S in NF@CS10-ZC-LDH4 plays an important role in redox reactions to boost the conductivity as well as the electrochemical durability of NF@CS10-ZC-LDH4.[57,58] According to the above interesting results, NF@CS10-ZC-LDH4 demonstrated prominent supercapacitive properties that were more optimal in comparison with previously published materials, as displayed in Table S1 (ESI†). The electrochemical results for NF@AC are shown in Fig. S13,† with capacitances of 184, 180.2, 175.7, 169, 154.5, and 145 F g^{-1} at 1, 2.5, 5, 7.5, 15, and 25 A g^{-1}, respectively.

Based on the remarkable supercapacitive features of NF@CS10-ZC-LDH4, a hybrid supercapacitor (NF@CS10-ZC-LDH4//NF@AC) was constructed using NF@CS10-ZC-LDH4 as the cathode electrode and NF@AC as the anode electrode, as shown in Fig. 7a. By making use of the highest voltage windows of NF@CS10-ZC-LDH4 (0.0 V to 0.6 V) and NF@AC (−1.0 to 0 V), an anticipated voltage window of NF@CS10-ZC-
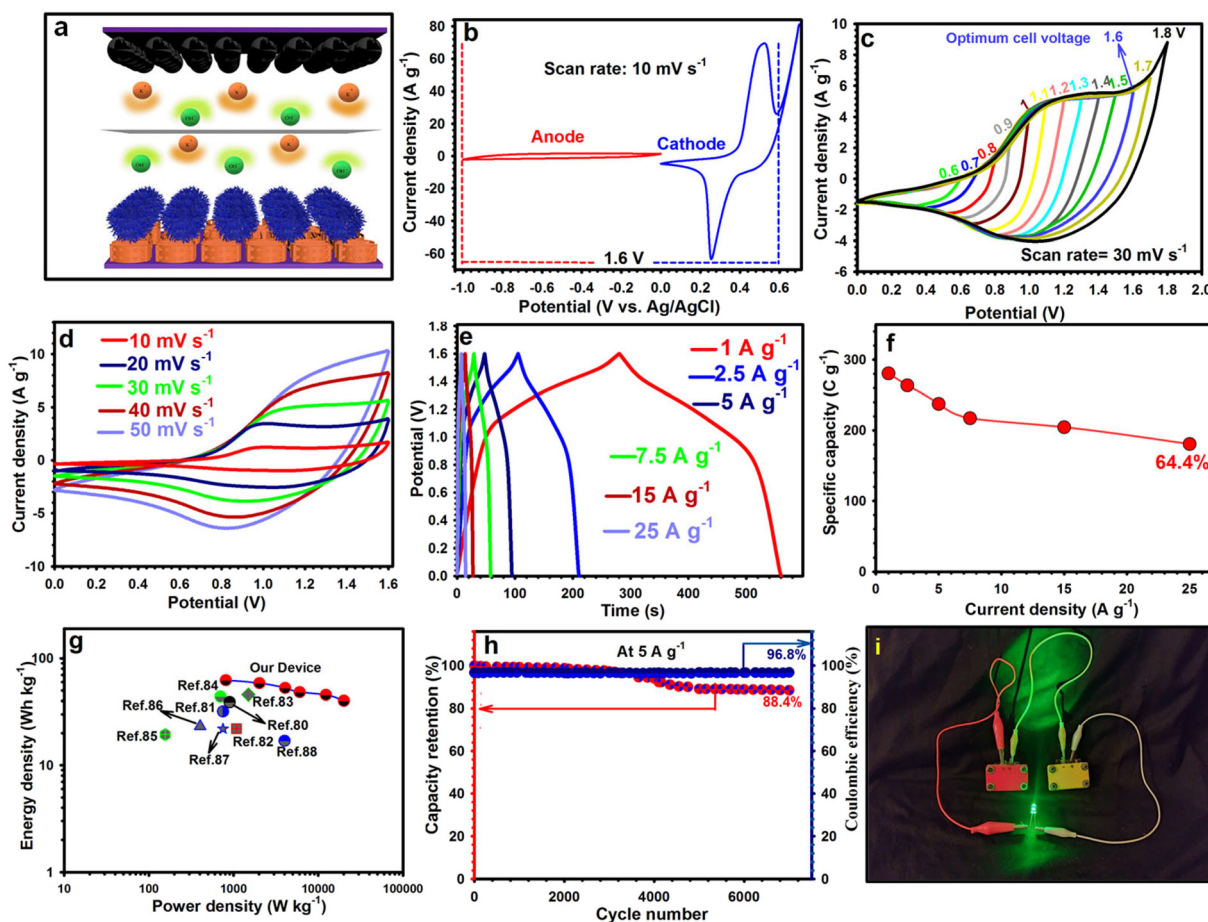

Fig. 7 (a) Schematic illustration of the NF@CS10-ZC-LDH4//NF@AC device. (b) CV plots for NF@AC and NF@CS10-ZC-LDH4 at 10 mV s^{-1} in a three-electrode cell. (c) CV plots for NF@CS10-ZC-LDH4 measured in several voltage windows at a scan rate of 30 mV s^{-1}. (d) CV plots for NF@CS10-ZC-LDH4//NF@AC at various sweep speeds of 10–50 mV s^{-1}. (e) GCD plots for NF@CS10-ZC-LDH4//NF@AC at various current densities of 1–25 A g^{-1}. (f) Specific capacity *vs.* current density for NF@CS10-ZC-LDH4//NF@AC. (g) A comparison of the NF@CS10-ZC-LDH4//NF@AC device's Ragone plot with various devices. (h) Durability and coulombic efficiency of NF@CS10-ZC-LDH4//NF@AC at 5 A g^{-1}. (i) Photograph of a green LED with two NF@CS10-ZC-LDH4//NF@AC devices.

LDH4//NF@AC was achieved at 1.60 V, as shown in Fig. 7b. Also, the CV profiles for NF@CS10-ZC-LDH4//NF@AC under diverse voltage windows at 30 mV s^{-1} in Fig. 7c show that weak polarization occurred at 1.7 V, thereby identifying that the optimized voltage window is 1.60 V for this apparatus. When the sweep speed was gradually increased from 10 to 50 mV s^{-1}, the shape of the graph displayed by NF@CS10-ZC-LDH4//NF@AC was roughly unchanged, implying satisfactory reversibility (Fig. 7d). The CV plots for NF@CS10-ZC-LDH4//NF@AC confirm the contribution of the electrochemical double layer capacitor (EDLC) and battery-type capacity derived from NF@AC and NF@CS10-ZC-LDH4, respectively.

To obtain the charge storage feature, including capacity, rate capability, energy, and power densities, the GCD plots (Fig. 7e) for NF@CS10-ZC-LDH4//NF@AC were recorded from 1 to 25 A g^{-1}. In the GCD curves, the charge/discharge times for NF@CS10-ZC-LDH4//NF@AC enabled satisfactory coulombic efficiency and reversibility due to their symmetrical nature. The capacities for NF@CS10-ZC-LDH4//NF@AC were estimated to be 280.55, 263.5, 237.6, 217.3, 204.6, and 180.7 C g^{-1} at 1, 2.5, 5, 7.5, 15, and 25 A g^{-1}, respectively, confirming 64.4% retention of the capacity (Fig. 7f).

The energy/power densities for NF@CS10-ZC-LDH4//NF@AC are also important for evaluating its performance, and thus, Fig. 7g shows a Ragone plot for NF@CS10-ZC-LDH4//NF@AC. The apparatus in our work possesses an E_d of 62.4 W h kg^{-1} at 810.4 W kg^{-1}. Moreover, even at 20080 W kg^{-1}, it continues to show an E_d of 40.16 W h kg^{-1}. Compared to published devices as shown in Fig. 7g, the E_d for NF@CS10-ZC-LDH4//NF@AC is better.[80–88] Remarkably, NF@CS10-ZC-LDH4//NF@AC maintained outstanding cyclability (88.4%) at 5 A g^{-1} even after 7000 cycles, and also a desired coulombic efficiency of 96.8% (Fig. 7h). To demonstrate the practicability of NF@CS10-ZC-LDH4//NF@AC, a green (2.9 V) light-emitting diode (LED) was easily lit (Fig. 7i) by connecting two NF@CS10-ZC-LDH4//NF@AC devices in series.

4 Conclusions

Porous CuS nanosheets coupled with flower-like ZnCo-LDH arrays supported on NF (NF@CS10-ZC-LDH4) were synthesized *via* two-step hydrothermal routes under morphology control. The porous structures formed by the combination of the CuS nanosheets and ZnCo-LDH nanoflowers promoted electrolyte infiltration, accelerated ion transfer, and relieved the stress produced during consecutive redox reactions. Additionally, the synergistic effect between CS10 and ZC-LDH4 greatly boosted the supercapacitive properties of NF@CS10-ZC-LDH4, resulting in a fabulous capacity of 1270.5 C g^{-1} and satisfactory cyclability of 90.7% after 7000 cycles. When the NF@CS10-ZC-LDH4 electrode was integrated into the hybrid device, it remarkably stored energy up to 62.4 W h kg^{-1} at 810.4 W kg^{-1}. These encouraging results might contribute to the development of efficient materials with low cost and high performance by controlling the morphology for supercapacitors.

Conflicts of interest

The authors declare no competing financial interests.

Acknowledgements

References

1 F. P. Perera, Multiple Threats to Child Health from Fossil Fuel Combustion: Impacts of Air Pollution and Climate Change, *Environ. Health Perspect.*, 2017, **125**, 141–148.

2 J. Wang, T. Ma, D. Ma, H. Li, L. Hua, Q. He and X. Deng, The Impact of Air Pollution on Neurodegenerative Diseases, *Ther. Drug Monit.*, 2021, **43**, 69–78.

3 H. Michaels, I. Benesperi and M. Freitag, Challenges and prospects of ambient hybrid solar cell applications, *Chem. Sci.*, 2021, **12**, 5002–5015.

4 Y. Zhu, H.-C. Chen, C.-S. Hsu, T.-S. Lin, C.-J. Chang, S.-C. Chang, L.-D. Tsai and H. M. Chen, Operando Unraveling of the Structural and Chemical Stability of P-Substituted CoSe$_2$ Electrocatalysts toward Hydrogen and Oxygen Evolution Reactions in Alkaline Electrolyte, *ACS Energy Lett.*, 2019, **4**, 987–994.

5 T. Zhao, C. Liu, T. Meng, W. Deng, L. Zheng, F. Yi, A. Gao and D. Shu, Graphene Quantum Dots Pinned on Nanosheet-Assembled NiCo-LDH Hollow Micro-Tunnels: Toward High-Performance Pouch-Type Supercapacitor via the Regulated Electron Localization, *Small*, 2022, **18**, 2201286.

6 S. Kiruthika, N. Sneha and R. Gupta, Visibly transparent supercapacitors, *J. Mater. Chem. A*, 2023, **11**, 4907–4936.

7 A. Mohammadi Zardkhoshoui, S. S. Hosseiny Davarani, M. Maleka Ashtiani and M. Sarparast, Designing an asymmetric device based on graphene wrapped yolk–double shell NiGa$_2$S$_4$ hollow microspheres and graphene wrapped FeS$_2$–FeSe$_2$ core–shell cratered spheres with outstanding energy density, *J. Mater. Chem. A*, 2019, **7**, 10282–10292.

8 A. Mohammadi Zardkhoshoui and S. S. Hosseiny Davarani, Formation of graphene-wrapped multi-shelled NiGa$_2$O$_4$ hollow spheres and graphene-wrapped yolk–shell NiFe$_2$O$_4$ hollow spheres derived from metal–organic frameworks for high-performance hybrid supercapacitors, *Nanoscale*, 2020, **12**, 1643–1656.

9 D. P. Dubal, O. Ayyad, V. Ruiz and P. Gómez-Romero, Hybrid energy storage: the merging of battery and supercapacitor chemistries, *Chem. Soc. Rev.*, 2015, **44**, 1777–1790.

10 J. Xie, P. Yang, Y. Wang, T. Qi, Y. Lei and C. M. Li, Puzzles and confusions in supercapacitor and battery: Theory and solutions, *J. Power Sources*, 2018, **401**, 213–223.

11 A. Mohammadi Zardkhoshoui and S. S. Hosseiny Davarani, Construction of complex copper-cobalt selenide hollow

© 2023 The Author(s). Co-published by the Institute of Process Engineering, Chinese Academy of Sciences and the Royal Society of Chemistry

Ind. Chem. Mater., 2023, **1**, 443–457 | **453**

structures as an attractive battery-type electrode material for hybrid supercapacitors, *Chem. Eng. J.*, 2020, **402**, 126241.

12 A. Mohammadi Zardkhoshoui, B. Ameri and S. S. Hosseiny Davarani, α-MnS@Co$_3$S$_4$ hollow nanospheres assembled from nanosheets for hybrid supercapacitors, *Chem. Eng. J.*, 2021, **422**, 129953.

13 B. Ameri, A. Mohammadi Zardkhoshoui and S. S. Hosseiny Davarani, Engineering of hierarchical NiCoSe$_2$@NiMn-LDH core-shell nanostructures as a high-performance positive electrode material for hybrid supercapacitors, *Sustainable Energy Fuels*, 2020, **4**, 5144–5155.

14 S. Guan, X. Fu, Z. Lao, C. Jin and Z. Peng, NiS-MoS$_2$ Heteronanosheet Arrays on Carbon Cloth for High-Performance Flexible Hybrid Energy Storage Devices, *ACS Sustainable Chem. Eng.*, 2019, **7**, 11672–11681.

15 A. Mohammadi Zardkhoshoui, B. Ameri and S. S. Hosseiny Davarani, Fabrication of hollow MnFe$_2$O$_4$ nanocubes assembled by CoS$_2$ nanosheets for hybrid supercapacitors, *Chem. Eng. J.*, 2022, **435**, 135170.

16 R. Arian, A. Mohammadi Zardkhoshoui and S. S. Hosseiny Davarani, Rational Construction of Core-Shell Ni−Mn−Co −S@Co(OH)$_2$ Nanoarrays toward High-Performance Hybrid Supercapacitors, *ChemElectroChem*, 2020, **7**, 2816–2825.

17 Y. Zhang, H. Chen, C. Guan, Y. Wu, C. Yang, Z. Shen and Q. Zou, Energy-Saving Synthesis of MOF-Derived Hierarchical and Hollow Co(VO$_3$)$_2$-Co(OH)$_2$ Composite Leaf Arrays for Supercapacitor Electrode Materials, *ACS Appl. Mater. Interfaces*, 2018, **10**, 18440–18444.

18 H. Tian, W. Bao, Y. Jiang, L. Wang, L. Zhang, O. Sha, C. Wu and F. Gao, Fabrication of Ni-Al LDH/nitramine-N-doped graphene hybrid composites via a novel self-assembly process for hybrid supercapacitors, *Chem. Eng. J.*, 2018, **354**, 1132–1140.

19 A. Mohammadi Zardkhoshoui, R. Hayati Monjoghtapeh and S. S. Hosseiny Davarani, Zn–Ni–Se@NiCo$_2$S$_4$ Core–Shell Architectures: A Highly Efficient Positive Electrode for Hybrid Supercapacitors, *Energy Fuels*, 2020, **34**, 14934–14947.

20 K. Alitabar, A. Mohammadi Zardkhoshoui and S. S. Hosseiny Davarani, One-Step Synthesis of Porous Ni− Co− Fe− S Nanosheet Arrays as an Efficient Battery-Type Electrode Material for Hybrid Supercapacitors, *Batteries Supercaps*, 2020, **3**, 1311–1320.

21 J. Xu, C. Xiang, S. Fang, L. Zhu, F. Xu, L. Sun, Y. Zou and J. Zhang, Template strategy to synthesize porous Mn-Co-S nanospheres electrode for high-performance supercapacitors, *J. Energy Storage*, 2021, **44**, 103267.

22 A. Dang, Y. Sun, Y. Liu, Y. Xia, X. Liu, Y. Gao, S. Wu, T. Li, A. Zada and F. Ye, Flexible Ti$_3$C$_2$T$_x$/Carbon Nanotubes/CuS Film Electrodes Based on a Dual-Structural Design for High-Performance All-Solid-State Supercapacitors, *ACS Appl. Energy Mater.*, 2022, **5**, 9158–9172.

23 X. Han, Y. Qin, J. Luo, F. Zhang and X. Lei, Polygonal CuS Nanoprisms Fabricated by Grinding Reaction for Advanced Quasi-Solid-State Asymmetry Supercapacitors, *ACS Appl. Energy Mater.*, 2021, **4**, 12631–12640.

24 W. Zhou, J. Miao, X. Yan, Y. Li, Y. Zhu, W. Zhang, M. Zhang, W. Zhu, M. S. Javed, J. Pan and S. Hussain, Boosted electrochemical performance of CuS anchored on carbon cloth as an integrated electrode for quasi-solid-state flexible supercapacitor, *J. Electroanal. Chem.*, 2021, **897**, 115610.

25 C. Li, P. He, L. Jia, X. Zhang, T. Zhang, F. Dong, M. He, S. Wang, L. Zhou, T. Yang and H. Liu, Facile synthesis of 3D CuS micro-flowers grown on porous activated carbon derived from pomelo peel as electrode for high-performance supercapacitors, *Electrochim. Acta*, 2019, **299**, 253–261.

26 K. Jin, M. Zhou, H. Zhao, S. Zhai, F. Ge, Y. Zhao and Z. Cai, Electrodeposited CuS nanosheets on carbonized cotton fabric as flexible supercapacitor electrode for high energy storage, *Electrochim. Acta*, 2019, **295**, 668–676.

27 A. Elgendy, N. M. El Basiony, F. El-Taib Heakal and A. E. Elkholy, Mesoporous Ni-Zn-Fe layered double hydroxide as an efficient binder-free electrode active material for high-performance supercapacitors, *J. Power Sources*, 2020, **466**, 228294.

28 X. Li, H. Wu, C. Guan, A. M. Elshahawy, Y. Dong, S. J. Pennycook and J. Wang, (Ni,Co)Se$_2$/NiCo-LDH Core/Shell Structural Electrode with the Cactus-Like (Ni,Co)Se$_2$ Core for Asymmetric Supercapacitors, *Small*, 2018, **15**, 1803895.

29 Z. Pan, Y. Jiang, P. Yang, Z. Wu, W. Tian, L. Liu, Y. Song, Q. Gu, D. Sun and L. Hu, In Situ Growth of Layered Bimetallic ZnCo Hydroxide Nanosheets for High- Performance All-Solid-State Pseudocapacitor, *ACS Nano*, 2018, **12**, 2968–2979.

30 Q. Zhang, B. Zhao, J. Wang, C. Qu, H. Sun and K. Zhang, High-performance hybrid supercapacitors based on self-supported 3D ultrathin porous quaternary Zn-Ni-Al-Co oxide nanosheets, *Nano Energy*, 2016, **28**, 475–485.

31 J. Tang, D. Liu, Y. Zheng, X. Li, X. Wang and D. He, Effect of Zn-substitution on cycling performance of α-Co(OH)$_2$ nanosheet electrode for supercapacitors, *J. Mater. Chem. A*, 2014, **2**, 2585–2591.

32 Z. H. Huang, F.-F. Sun, M. Batmunkh, W.-H. Li, H. Li, Y. Sun, Q. Zhao, X. Liu and T.-Y. Ma, Zinc–nickel–cobalt ternary hydroxide nanoarrays for high-performance supercapacitors, *J. Mater. Chem. A*, 2019, **7**, 11826–11835.

33 M. H. Lee, P. Bandyopadhyay, E. M. Jin, E. Baasanjav, D.-W. Kang and S. M. Jeong, Cathode of Zn-Ni Layered Double Hydroxide Nanosheet Arrays Wrapped with a Porous NiMoS$_x$ Shell and Anode of 3D Hierarchical Nitrogen-Doped Carbon for High-Performance Asymmetric Supercapacitors, *ACS Appl. Energy Mater.*, 2021, **4**, 9166–9177.

34 L. Li, H. Yang, J. Yang, L. Zhang, J. Miao, Y. Zhang, C. Sun, W. Huang, X. Dong and B. Liu, Hierarchical carbon@Ni$_3$S$_2$@MoS$_2$ double core–shell nanorods for high-performance supercapacitors, *J. Mater. Chem. A*, 2016, **4**, 1319–1325.

35 P. Qin, X. Li, B. Gao, J. Fu, L. Xia, X. Zhang, K. Huo, W. Shen and P. K. Chu, Hierarchical TiN nanoparticles-assembled nanopillars for flexible supercapacitors with high volumetric capacitance, *Nanoscale*, 2018, **10**, 8728–8734.

36 R. Hayati Monjoghtapeh, A. Mohammadi Zardkhoshoui and S. S. Hosseiny Davarani, Hierarchical MnCo$_2$S$_4$ nanowires/

NiFeLDH nanosheets/graphene: a promising binder-free positive electrode for high-performance supercapacitors, *Electrochim. Acta*, 2020, **338**, 135891.

37 M. Amiri, A. Mohammadi Zardkhoshoui, S. S. Hosseiny Davarani, M. Maghsoudi and M. K. Altafi, A high-performance hybrid supercapacitor by encapsulating binder-less FeCoSe$_2$ nanosheets@ NiCoSe$_2$ nanoflowers in a graphene network, *Sustainable Energy Fuels*, 2022, **6**, 3626–3642.

38 Y. Yang, W. Huang, S. Li, L. Ci and P. Si, Surfactant-dependent flower- and grass-like Zn$_{0.76}$Co$_{0.24}$S/Co$_3$S$_4$ for high-performance all-solid-state asymmetric supercapacitors, *J. Mater. Chem. A*, 2018, **6**, 22830–22839.

39 A. Mohammadi Zardkhoshoui and S. S. Hosseiny Davarani, Ultra-high energy density supercapacitors based on metal–organic framework derived yolk–shell Cu–Co–P hollow nanospheres and CuFeS$_2$ nanosheet arrays, *Dalton Trans.*, 2020, **49**, 10028–10041.

40 M. Li, M. Zhou, Z. Q. Wen and Y. X. Zhang, Flower-like NiFe layered double hydroxides coated MnO$_2$ for high-performance flexible supercapacitors, *J. Energy Storage*, 2017, **11**, 242–248.

41 M. A. Raza, N. Iqbal, T. Noor and Z. A. Ghazi, Hierarchical Flower-like NiMn-LDH@MnCo$_2$S$_4$ Grown on Nickle Foam as a High-Specific Capacity Faradaic Electrode, *Energy Fuels*, 2023, **37**, 1310–1317.

42 Y. Qian, J. Zhang, J. Jin, S. Yang and G. Li, Flexible Solid-State Asymmetric Supercapacitor with High Energy Density and Ultralong Lifetime Based on Hierarchical 3D Electrode Design, *ACS Appl. Energy Mater.*, 2022, **5**, 5830–5840.

43 S. C. Sekhar, B. Ramulu, S. J. Arbaz, S. K. Hussain and J. S. Yu, One-Pot Hydrothermal- Derived NiS$_2$–CoMo$_2$S$_4$ with Vertically Aligned Nanorods as a Binder-Free Electrode for Coin-Cell-Type Hybrid Supercapacitor, *Small Methods*, 2021, **5**, 2100335.

44 X. Yang, Y. Tian, S. Li, Y.-P. Wu, Q. Zhang, D.-S. Li and S. Zhang, Heterogeneous Ni-MOF/V$_2$CT$_x$–MXene hierarchically-porous nanorods for robust and high energy density hybrid supercapacitors, *J. Mater. Chem. A*, 2022, **10**, 12225–12234.

45 L. Wan, Y. Wang, Y. Zhang, C. Du, J. Chen, Z. Tian and M. Xie, FeCoP nanosheets@Ni-Co carbonate hydroxide nanoneedles as free-standing electrode material for hybrid supercapacitors, *Chem. Eng. J.*, 2021, **415**, 128995.

46 V. Singh, A. Tiwari and T. C. Nagaiah, Facet-controlled morphology of cobalt disulfide towards enhanced oxygen reduction reaction, *J. Mater. Chem. A*, 2018, **6**, 22545–22554.

47 Y. Lu, B. Jiang, L. Fang, F. L. Ling, F. Wu, B. S. Hu, F. M. Meng, K. Y. Niu, F. Lin and H. M. Zheng, An investigation of ultrathin nickel-iron layered double hydroxide nanosheets grown on nickel foam for high performance supercapacitor electrodes, *J. Alloys Compd.*, 2017, **714**, 63–70.

48 X. Tan, Z. Feng, W. Yang, H. Zou and S. Chen, Flower-like Heterogeneous Phosphorus-Doped Co$_3$S$_4$@Ni$_3$S$_4$ Nanoparticles as a Binder-free Electrode for Asymmetric All-Solid-State Supercapacitors, *ACS Appl. Energy Mater.*, 2023, **6**, 702–713.

49 Q. Lu, S. Zhou, M. Chen, B. Li, H. Wei, B. Zi, Y. Zhang, J. Zhang and Q. Liu, Hybrid cobalt–manganese oxides prepared by ordered steps with a ternary nanosheet structure and its high performance as a binder-free electrode for energy storage, *Nanoscale*, 2021, **13**, 2573–2584.

50 L. Mi, W. Wei, Z. Zheng, Y. Gao, Y. Liu, W. Chen and X. Guan, Tunable properties induced by ion exchange in multilayer intertwined CuS microflowers with hierarchal structures, *Nanoscale*, 2013, **5**, 6589–6598.

51 C. Qiu, F. Cai, Y. Wang, Y. Liu, Q. Wang and C. Zhao, 2-Methylimidazole directed ambient synthesis of zinc-cobalt LDH nanosheets for efficient oxygen evolution reaction, *J. Colloid Interface Sci.*, 2020, **565**, 351–359.

52 C. Wang, W. Wu, C. Zhao, T. Liu, L. Wang and J. Zhu, Rational design of 2D/1D ZnCo-LDH hierarchical structure with high rate performance as advanced symmetric supercapacitors, *J. Colloid Interface Sci.*, 2021, **602**, 177–186.

53 Z. Shi, J. Zhu, Z. Li, Q. Xiao and J. Zhu, Sulfur-Doped Nickel–Cobalt Double Hydroxide Electrodes for High-Performance Asymmetric Supercapacitors, *ACS Appl. Energy Mater.*, 2020, **3**, 11082–11090.

54 Z. Jin, X. Wang, Y. Wang, T. Yan and X. Hao, Snowflake-like Cu$_2$S Coated with NiAl-LDH Forms a p–n Heterojunction for Efficient Photocatalytic Hydrogen Evolution, *ACS Appl. Energy Mater.*, 2021, **4**, 14220–14231.

55 A. Mohammadi Zardkhoshoui, B. Ameri and S. S. Hosseiny Davarani, A high-energy-density supercapacitor with multi-shelled nickel–manganese selenide hollow spheres as cathode and double-shell nickel–iron selenide hollow spheres as anode electrodes, *Nanoscale*, 2021, **13**, 2931–2945.

56 A. Mohammadi Zardkhoshoui and S. S. Hosseiny Davarani, Boosting the energy density of supercapacitors by encapsulating a multi-shelled zinc–cobalt-selenide hollow nanosphere cathode and a yolk–double shell cobalt–iron-selenide hollow nanosphere anode in a graphene network, *Nanoscale*, 2020, **12**, 12476–12489.

57 A. Mohammadi Zardkhoshoui and S. S. Hosseiny Davarani, An efficient hybrid supercapacitor based on Zn–Mn–Ni–S@NiSe core–shell architectures, *Sustainable Energy Fuels*, 2021, **5**, 900–913.

58 A. Mohammadi Zardkhoshoui, M. Maleka Ashtiani, M. Sarparast and S. S. Hosseiny Davarani, Enhanced the energy density of supercapacitors via rose-like nanoporous ZnGa$_2$S$_4$ hollow spheres cathode and yolk-shell FeP hollow spheres anode, *J. Power Sources*, 2020, **450**, 227691.

59 R. J. Gilliam, J. W. Graydon, D. W. Kirk and S. J. Thorpe, A review of specific conductivities of potassium hydroxide solutions for various concentrations and temperatures, *Int. J. Hydrogen Energy*, 2007, **32**, 359–364.

60 W. Jiang, F. Hu, Q. Yan and X. Wu, Investigation on electrochemical behaviors of NiCo$_2$O$_4$ battery-type supercapacitor electrodes: the role of an aqueous electrolyte, *Inorg. Chem. Front.*, 2017, **4**, 1642–1648.

61 B. Ameri, A. Mohammadi Zardkhoshoui and S. S. Hosseiny Davarani, An advanced hybrid supercapacitor constructed

© 2023 The Author(s). Co-published by the Institute of Process Engineering, Chinese Academy of Sciences and the Royal Society of Chemistry

Ind. Chem. Mater., 2023, **1**, 443–457 | **455**

from rugby-ball-like $NiCo_2Se_4$ yolk–shell nanostructures, *Mater. Chem. Front.*, 2021, **5**, 4725–4738.

62 A. Mohammadi Zardkhoshoui, S. S. Hosseiny Davarani and A. A. Asgharinezhad, Designing graphene-wrapped $NiCo_2Se_4$ microspheres with petal-like FeS_2 toward flexible asymmetric all-solid-state supercapacitors, *Dalton Trans.*, 2019, **48**, 4274–4282.

63 P. Bandyopadhyay, G. Saeed, N. H. Kim, S. M. Jeong and J. H. Lee, Fabrication of Hierarchical Zn–Ni–Co–S Nanowire arrays and Graphitic Carbon Nitride/Graphene for Solid-State Asymmetric Supercapacitors, *Appl. Surf. Sci.*, 2021, **542**, 148564.

64 P. Bandyopadhyay, G. Saeed, N. H. Kim and J. H. Lee, Zinc-nickel-cobalt oxide@$NiMoO_4$ core-shell nanowire/nanosheet arrays for solid state asymmetric supercapacitors, *Chem. Eng. J.*, 2020, **384**, 123357.

65 Y. Qin, Q. Du, J. Deng, J. Zou, G. Lu and P. Wang, Electronic Structure Modulation and Phase Transformation of Nickel–Cobalt Carbonate Hydroxide Caused by Halogen Doping and Its Effect on Supercapacitor Performance, *ACS Appl. Energy Mater.*, 2022, **5**, 469–480.

66 L. Mei, T. Yang, C. Xu, M. Zhang, L. Chen, Q. Li and T. Wang, Hierarchical mushroom-like CoNi2S4 arrays as a novel electrode material for supercapacitors, *Nano Energy*, 2014, **3**, 36–45.

67 Z. Pan, F. Cao, X. Hu and X. Ji, A facile method for synthesizing CuS decorated Ti_3C_2 MXene with enhanced performance for asymmetric supercapacitors, *J. Mater. Chem. A*, 2019, **7**, 8984–8992.

68 Y. Ma, J. Hao, H. Liu, W. Shi and J. Lian, Facile synthesis clusters of sheet-like Ni_3S_4/CuS nanohybrids with ultrahigh supercapacitor performance, *J. Solid State Chem.*, 2020, **282**, 121088.

69 C. Wang, Z. Liu, Y. Sun, X. Liu, Y. Wang and J. Liu, Honeycomb-like $MgCo_2O_4$@ZnCo layered double hydroxide as novel electrode material for high-performance all-solid-state supercapacitors, *Appl. Surf. Sci.*, 2023, **612**, 155661.

70 C. Kang, L. Ma, Y. Chen, L. Fu, Q. Hu, C. Zhou and Q. Liu, Metal-organic framework derived hollow rod-like NiCoMn ternary metal sulfide for high-performance asymmetric supercapacitors, *Chem. Eng. J.*, 2022, **427**, 131003.

71 I. Hussain, T. Hussain, S. Yang, Y. Chen, J. Zhou, X. Ma, N. Abbas, C. Lamiel and K. Zhang, Integration of CuO nanosheets to Zn-Ni-Co oxide nanowire arrays for energy storage application, *Chem. Eng. J.*, 2021, **413**, 127570.

72 Y. Wang, F. Xu, F. Zhou, L. Dai, K. Qu, Y. Wu, S. Gu and Z. Xu, Room-Temperature Synthesis of NiCo-Layered Double Hydroxide/MXene Composites for High-Performance Supercapacitors, *Ind. Eng. Chem. Res.*, 2022, **61**, 8800–8808.

73 Z. Ma, L. Fan, F. Jing, J. Zhao, Z. Liu, Q. Li, J. Li, Y. Fan, H. Dong, X. Qin and G. Shao, MnO_2 Nanowires@NiCo-LDH Nanosheet Core–Shell Heterostructure: A Slow Irreversible Transition of Hydrotalcite Phase for High-Performance Pseudocapacitance Electrode, *ACS Appl. Energy Mater.*, 2021, **4**, 3983–3992.

74 C. Wang, H. Tian, J. Jiang, T. Zhou, Q. Zeng, X. R. He, P. Huang and Y. Yao, Facile Synthesis of Different Morphologies of Cu_2SnS_3 for High-Performance Supercapacitors, *ACS Appl. Mater. Interfaces*, 2017, **9**, 26038–26044.

75 X. Ma, S. Wang, H. Wang, J. Ding, S. Liu, Z. Huang, W. Sun, G. Liu, L. Wang and W. Xu, Construction of high-performance asymmetric supercapacitor based on FeCo-LDH@C_3N_4 composite electrode material with penetrating structure, *J. Energy Storage*, 2022, **56**, 106034.

76 W. Tang, J. Bai, P. Zhou, Q. He, F. Xiao, M. Zhao, P. Yang, L. Liao, Y. Wang, P. He, B. Jia and L. Bian, Polymethylene blue nanospheres supported honeycomb-like NiCo-LDH for high-performance supercapacitors, *Electrochim. Acta*, 2023, **439**, 141683.

77 K. Zhang, H.-Y. Zeng, H.-B. Li, S. Xu, S.-B. Lv and M.-X. Wang, Controllable preparation of $CuCo_2S_4$ nanotube arrays for high-performance hybrid supercapacitors, *Electrochim. Acta*, 2022, **404**, 139681.

78 H.-B. Li, G.-F. Xiao, H.-Y. Zeng, X.-J. Cao, K.-M. Zou and S. Xu, Supercapacitor based on the $CuCo_2S_4$@NiCoAl hydrotalcite array on Ni foam with high-performance, *Electrochim. Acta*, 2020, **352**, 136500.

79 S. Alkhalaf, C. K. Ranaweera, P. K. Kahol, K. Siam, H. Adhikari, S. R. Mishra, F. Perez, B. K. Gupta, K. Ramasamy and R. K. Gupta, Electrochemical energy storage performance of electrospun $CoMn_2O_4$ nanofibers, *J. Alloys Compd.*, 2017, **692**, 59–66.

80 H. Li, Z. Li, Z. Wu, M. Sun, S. Han, C. Cai, W. Shen, X. Teng, L. Yong and Q. Fu, Enhanced electrochemical performance of $CuCo_2S_4$/carbon nanotubes composite as electrode material for supercapacitors, *J. Colloid Interface Sci.*, 2019, **549**, 105–113.

81 P. Naveenkumar and G. P. Kalaignan, Fabrication of core-shell like hybrids of $CuCo_2S_4$@NiCo(OH)$_2$ nanosheets for supercapacitor applications, *Composites, Part B*, 2019, **173**, 106864.

82 Z. Tian, X. Wang, B. Li, H. Li and Y. Wu, High rate capability electrode constructed by anchoring CuCo2S4 on graphene aerogel skeleton toward quasi-solid-state supercapacitor, *Electrochim. Acta*, 2019, **298**, 321–329.

83 J. Lin, H. Jia, H. Liang, S. Chen, Y. Cai, J. Qi, C. Qu, J. Cao, W. Fei and J. Feng, Hierarchical CuCo2S4@NiMn-layered double hydroxide core-shell hybrid arrays as electrodes for supercapacitors, *Chem. Eng. J.*, 2018, **336**, 562–569.

84 Y. Yuan, H. Jia, Z. Liu, L. Wang, J. Sheng and W. Fei, A highly conductive Ni(OH)$_2$ nano-sheet wrapped $CuCo_2S_4$ nano-tube electrode with a core–shell structure for high performance supercapacitors, *Dalton Trans.*, 2021, **50**, 8476–8486.

85 J. Yuan, L. Jiang, J. Che, G. He and H. Chen, Composites of NiS_2 Microblocks, MoS_2 Nanosheets, and Reduced Graphene Oxide for Energy Storage and Electrochemical Detection of Bisphenol A, *ACS Appl. Nano Mater.*, 2021, **4**, 6093–6102.

86 Z. Dai, L. Xue, Z. Zhang, Y. Gao, J. Wang, Q. Gao and D. Chen, Construction of Single-Phase Nickel Disulfide Microflowers as High-Performance Electrodes for Hybrid Supercapacitors, *Energy Fuels*, 2020, **34**, 10178–10187.

87 L. Qiu, W. Yang, Q. Zhao, S. Lu, X. Wang, M. Zhou, B. Tao, Q. Xie and Y. Ruan, NiS Nanoflake-Coated Carbon Nanofiber Electrodes for Supercapacitors, *ACS Appl. Nano Mater.*, 2022, **5**, 6192–6200.

88 H. Wang, J. Wang, M. Liang, Z. He, K. Li, W. Song, S. Tian, W. Duan, Y. Zhao and Z. Miao, Novel Dealloying-Fabricated NiS/NiO Nanoparticles with Superior Cycling Stability for Supercapacitors, *ACS Omega*, 2021, **6**, 17999–18007.

© 2023 The Author(s). Co-published by the Institute of Process Engineering, Chinese Academy of Sciences and the Royal Society of Chemistry

Ind. Chem. Mater., 2023, **1**, 443–457 | **457**